Surface & Coatings Technology 433 (2022) 128134

Contents lists available at ScienceDirect

Surface & Coatings Technology

journal homepage: www.elsevier.com/locate/surfcoat

A comparative study on high-temperature air oxidation of Cr-coated E110 zirconium alloy deposited by magnetron sputtering and electroplating

D.V. Sidelev [a,*], C. Poltronieri [b,c], M. Bestetti [a,b], M.G. Krinitcyn [a,d], V.A. Grudinin [a], E. B. Kashkarov [a]

[a] National Research Tomsk Polytechnic University, School of Nuclear Science and Engineering, 634050 Tomsk, Russia
[b] Politecnico di Milano, Department of Chemistry, Materials and Chemical Engineering "Giulio Natta", 20133 Milano, Italy
[c] Laboratoire des Sciences des Procédés des Matériaux, CNRS 3407, Université Sorbonne Paris Nord, France
[d] Institute of Strength Physics and Materials Science, Siberian Branch, Russian Academy of Sciences, 634055 Tomsk, Russia

ARTICLE INFO

Keywords:
High-temperature oxidation
Chromium coatings
Zirconium alloys
Magnetron sputtering
Electroplating

ABSTRACT

Chromium coatings were deposited either by magnetron sputtering and electroplating on E110 zirconium alloy. The as-deposited Cr coatings showed dense microstructure, but different mechanical properties and adhesion behavior depending on the deposition technology. High-temperature oxidation was performed in air at 1100 °C for 40 min. The magnetron-deposited coatings had a stable oxidation behavior which was improved by increasing coating thickness. Surface activation of E110 alloy prior to Cr electroplating resulted in formation of the interlayer with a thickness of 7–12 μm between the coating and the alloy containing hydride and fluoride phases. It was shown that cracks and defects in this interlayer of the electroplated Cr coatings affected the coating adhesion and resulted in lower oxidation resistance compared to the magnetron-deposited coatings.

1. Introduction

The severe event occurred at Fukushima Daiichi Nuclear Power Plant in 2011 [1] showed an important weakness in zirconium nuclear fuel claddings. The exposure of Zr claddings to high-temperature water steam resulted in the exothermic ($\Delta H^\circ = -584.5$ kJ/mol at 1200 °C) oxidation reaction:

$$Zr + 2{\cdot}H_2O(g) \rightarrow ZrO_2 + 2{\cdot}H_2(g) + \Delta H \quad (1)$$

A serious problem was additionally related to hydrogen generation which damaged the reactor buildings with the subsequent release of highly radioactive fission products [2]. Nowadays, accident-tolerant fuels (ATF) are of global interest and investigated by many research institutions and industrial companies, e.g., CEA (France), ROSATOM (Russia), CTU Prague (Czech Republic), KIT (Germany), Korea Atomic Energy Research Institute, etc. [3–8].

The short-term strategy of ATF suggests protective coating deposition on Zr alloy claddings. Currently, numerous film types are studied such as metallic (Cr, Cr—Al, Ni—Cr, etc.), non-metallic (oxides, carbides and nitrides) or compound and multilayer coatings (CrN/Cr, ZrO_2/Cr, CrN/TiN, etc.) [9–19]. According to literature, chromium is a one of the most promising candidate among other coating materials due to the protective Cr_2O_3 scale formed on surface of Cr-coated Zr claddings under high-temperature oxidation [3–4,20–24]. Recent studies showed that thick (~10 μm or more) dense and columnar-free microstructure Cr coatings can be protective for a long-time in loss of coolant accident (LOCA) scenarios [4–5,24].

Nowadays, most studies are focused on coating technologies for film deposition on Zr alloy claddings [3–4,6,25–27]. A wide variety of methods was applied to deposit protective coatings on Zr alloys such as magnetron sputtering, cathodic arc deposition, cold spraying, 3D laser cladding, electroplating [28–32], etc. Among them, PVD technologies are beneficial and advantageous for ATF cladding production due to high adhesion, dense microstructure and high purity of the deposited coatings. For example, Brachet et al. deposited columnar-free and dense Cr coatings by the energetic magnetron sputtering [3]. The multi-cathode magnetron sputtering system with "closed" magnetic field was used to deposit dense Cr coating which was protective for the base material in LOCA oxidation conditions at 1200 °C for 10 min [24]. Moreover, the multilayer Cr-based coating with high oxidation resistance was obtained by filtered vacuum-arc evaporation [33]. However, PVD technologies are expensive and have a low productivity since the

* Corresponding author.
E-mail address: sidelevdv@tpu.ru (D.V. Sidelev).

https://doi.org/10.1016/j.surfcoat.2022.128134
Received 4 February 2021; Received in revised form 3 January 2022; Accepted 17 January 2022
Available online 21 January 2022

typical deposition rates are in the range of ~1–10 nm/s (taking into account only deposition time) depending on coating technology and installation type [34]. Thus, increasing the efficiency of PVD methods or using other coating technologies with higher productivity to deposit thick and dense Cr coatings is also relevant [24,35–37].

Opposite to PVD technologies, electroplating has high productivity, simplicity of equipment and low operating costs. However, the limit of Cr electroplating for development of ATF Zr-based claddings is given by the presence of superficial tenacious oxides due to rapid passivation of zirconium alloys [38]. Proper activation procedures were developed to dissolve the superficial passivation layer and to limit its further formation preventing the surface oxidation of Zr alloys. For example in [39], a three-stage pretreatment of Zr-4 alloy was applied to deposit Cr coatings on Zr alloy by electroplating. The pretreatment includes an activation step in an acidic ammonium bifluoride solution, electroplating of Ni and high-temperature heating (750 °C, 10 min in protective Ar atmosphere. However, we earlier showed the detrimental effect of Ni content in protective coatings for Zr alloys at high-temperature oxidation [20]. Moreover, mechanical properties of Zr alloys can be affected by the high-temperature treatment. At present, there are only few articles which succeed in electroplating of chromium coatings on Zr alloys with/without intermediate layers, but thermal treatment was applied in all studies [38–41]. However, post-heat treatment can affect mechanical properties and corrosion resistance of Zr alloys [42] as the annealing temperature of the commercially used Zr claddings is about 500 °C [43]. So, it is important to understand high-temperature oxidation behavior of zirconium alloys with electroplating Cr coatings without any sublayer and post-heat treatment.

The aim of this work is to electroplate Cr coatings on Zr alloy without interlayer, to investigate and to compare their high-temperature oxidation resistance with those of Cr coatings deposited by PVD technology (magnetron sputtering).

2. Materials and methods

2.1. Cr coating deposition

Electroplating and magnetron sputtering were applied to obtain Cr coatings on E110 (0.9–1.1 wt% Nb, 0.06–0.1 wt% O, Zr balance) zirconium alloy. Before deposition, the samples of the E110 alloy with a size of 15 × 15 × 2 mm^3 were grinded and polished by a SiC sandpaper (Kemet Europe BV, UK) with P400 → P2500 grades and then degreased with acetone.

For Cr electroplating, a two-step activation process was adopted: firstly, the substrates were pickled in 1 l aqueous solution containing 100 ml HNO_3 (65%) and 100 ml HF (40%) at room temperature for 3 min, and then rinsed with distilled water; subsequently, the samples were immersed in an aqueous solution containing 18 g/l $NaHF_2$ and 2 ml/l H_2SO_4 (96%) at room temperature for 1 min, and then rinsed with distilled water. The electroplating was performed in 300 ml bath containing 75.9 g CrO_3, 0.6 ml H_2SO_4 (96%), 1.5 ml HF (40%) and distilled water. The distance between the cathode (E110 alloy) and Pb anode was ~4 cm. The electroplating parameters are reported in Table 1. Several experiments were performed to identify the most appropriated conditions, when the electroplated Cr coating was more adherent to E110 alloy and had a dense microstructure.

Table 1
- The parameters of Cr electroplating.

#	t_{dep}, min	j, A/cm^2	η, %	h, μm
E5	40		9	5.5
E11	60	0.21	12	11.0
E15	70		13	15.0

Note: t_{dep} – deposition time; j – current density; η – cathodic current efficiency; h – coating thickness.

The Cr electroplating was carried out by varying the solution temperature during the process: the solution was maintained at room temperature for 10 min and after, it was gradually heated up to 50 °C (Fig. 1).

For magnetron deposition of Cr coatings, the ion-plasma installation [20] with a multi-cathode magnetron sputtering system was used to deposit Cr coatings onto the E110 alloy. The magnetron system was equipped with Cr (99.95%) target disks and had a direct current (DC) power supply of APEL-M series (JSC "Applied electronics", Tomsk, Russia).

Before deposition, the samples were etched by Ar ions (voltage 2.5 kV, ion current 45 mA, pressure 0.15 Pa) for 30 min to remove surface oxides and contaminations. The substrate was biased at −600 V (pulse frequency 100 kHz). The samples were heated up to 200 °C during the pretreatment stage. An infrared pyrometer Optris CT laser 3MH1CF4 (Optris GmbH, Germany) was used to measure the temperature of the substrates. The samples were planetary rotated during both pretreatment and coating deposition. The magnetron sputtering parameters are shown in Table 2. The deposition conditions of Cr coatings on E110 alloy were selected in view of the analysis of our previous studies [20,24,35].

2.2. Oxidation test

The oxidation test was carried out in air atmosphere. The furnace ATS 3210 (Applied Test Systems Inc., USA) with temperature control system ATS AB-900 was used. The samples were fixed to a ceramic holder in the furnace using a quartz wire. The oxidation test is composed by the following steps:

- introduction of the sample in the furnace at 500 °C and heating up to 1100 °C with a heating rate of ~21 °C/min;
- isothermal treatment at 1100 °C for 40 min;
- cooling from 1100 to 500 °C with a rate of ~16 °C/min;
- extraction of the samples and cooling to room temperature.

An uncoated E110 alloy sample was also oxidized in the above mentioned conditions to perform a comparative analysis.

2.3. Sample characterization

Thicknesses and cross-sections of the as-deposited Cr coatings were analyzed by scanning electron microscope (SEM) S-3400 N (Hitachi, Japan) with back-scattered electrons detector and energy dispersive spectroscopy (EDS) attachment Bruker XFlash 4010/5010. Crystal structure was studied by using an X-ray diffractometer (XRD) XRD-7000S (Shimadzu, Japan) in a Bragg-Brentano configuration with

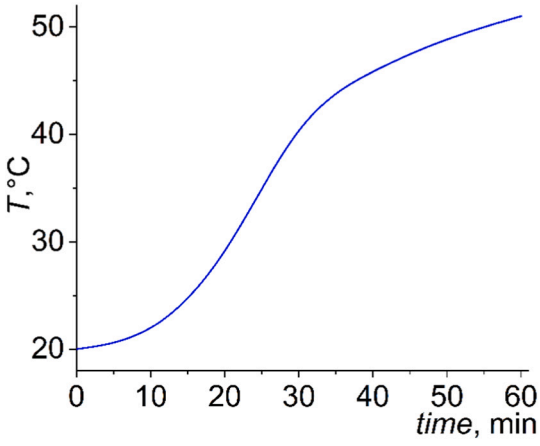

Fig. 1. The temperature profile in the bath during the electroplating of Cr on E110 samples.

Table 2
– The parameters of magnetron sputtering.

#	Q, W/cm^2	T_{sub}, °C	P, Pa	h, μm	U_{bias}, V (100 kHz, σ – 1.4)	j_{sub}, A/cm^2
M4.5		215		4.5		0.08
M6	39.3	218	0.2	6.0	−100	0.09
M8.2		224		8.2		0.09

Note: Q – target power density; T_{sub} – substrate temperature; P – operation pressure; U_{bias} – pulsed substrate bias; σ – duty cycle of pulse; j_{sub} – ion current density on the substrate.

CuKα-tube (40 kV, 30 mA). Texture coefficients $T_c(hkl)$ of the Cr coatings were calculated using the formula [44]:

$$T_c(hkl) = \frac{I(hkl)/I_0(hkl)}{1/N \cdot \sum_N \left(I(hkl)/I_0(hkl) \right)}, \quad (1)$$

where $I(hkl)$ – the measured intensity, $I_0(hkl)$ – the relative intensity of the reflection according to the powder standard (JCPDS), and N – the number of reflections. Moreover, residual stress in the Cr coatings was evaluated using by the $\sin^2\psi$ method using the X-ray diffractometer (Shimadzu XRD-7000S) with CuKα-radiation. The Cr (110), Cr (200) and Cr (211) peaks were selected to evaluate residual stresses in the incident angle range of 0–40°.

Hardness and elastic modulus of the coatings were investigated by a scanning nanoindenter Nanoscan-3D (FSBI «TISNCM», Russia) with a Berkovich indenter tip, and to reduce the experimental error, 20 indentations were carried out for each sample. The indentation depth was equal to ~10% of the coating thickness. Adhesion tests of the as-deposited Cr coatings were carried out by a Micro Scratch Tester T-S-AX-0000 (CSEM, Switzerland) with C-029 Rockwell indenter (radius 100 μm). The applied load was increased up to 30 N in 1 min and the scratch length was 7 mm. Weight of the samples before and after high-temperature oxidation test was measured using an analytical balance (Sartorius CP124 S) with an accuracy of 10^{-4} g. Cross-section microstructure of the samples after oxidation was studied by SEM and optical microscopy using AXIOVERT 200MAT (Zeiss, Germany). The elemental distributions of the samples with electroplated Cr coatings on depth were investigated before and after the oxidation test by a glow discharge optical emission spectroscopy (GDOES) using GD-Profiler 2 (HORIBA Scientific, Kyoto, Japan). The characterization of the samples was carried out using the equipment of the Center for Sharing Use «Nanomaterials and Nanotechnologies» of Tomsk Polytechnic University supported by the RF Ministry of Education and Science.

3. Results

3.1. As-deposited Cr coatings

Fig. 2 shows the cross-sections of the Cr-coated E110 obtained by electroplating and magnetron sputtering at different magnifications.

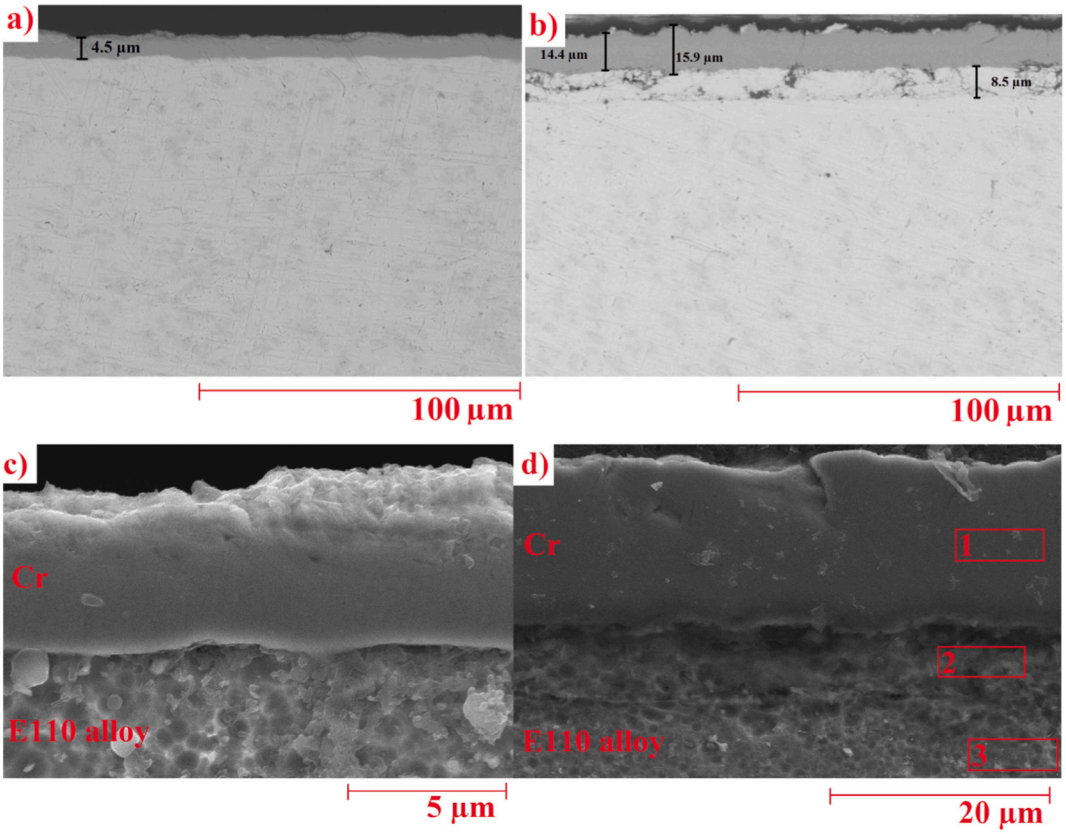

in at.%	F	Na	Cr	Zr
zone 1	0.00	0.00	99.78	0.22
zone 2	4.52	1.27	12.27	81.94
zone 3	3.06	0.58	0.12	96.24

Fig. 2. SEM images of the cross-section microstructure of E110 alloy with the as-deposited Cr coatings obtained by (a, c) magnetron sputtering and (b, d) electroplating.

Both coatings have a dense microstructure across the whole thickness of the samples. A uniform and well defined interface between the E110 alloy and Cr coating is observed in the case of magnetron sputtering (Fig. 2,a). The magnetron-deposited coatings show a smooth surface and a uniform thickness over their cross-sections, while the thickness of the electroplated coatings are non-uniform (e.g. 13.8–16.2 μm for the #E3 sample). This inhomogeneity of the thickness is due to the uneven current density distribution on small size samples during the electroplating process. Moreover, defects were observed at the "coating-alloy" interface in the case of electroplated Cr. A layer (~8–12 μm) with cracks and pores was found underneath the electroplated Cr coating over its whole cross-section (Fig. 2,b). The Fig. 2,c and 2,d show the cross-section microstructure of the samples after etching treatment at higher magnification to reveal the microstructure features. To investigate the change of elemental composition of the E110 alloy due to surface activation during the electroplating process, EDS analysis was performed at different depths in both Cr coating and E110 alloy. Apart from Zr, the Na (1.3 at.%) and F (4.5 at.%) signals were found underneath the electroplated Cr coating in the E110 alloy. However, the concentrations of Na and F are near the measurement limit of EDS technique. So, the obtained results should be considered only in a qualitative way. The content of F and Na decreased to 3.1 and 0.6 at.%, respectively, at higher depth in the alloy.

Fig. 3 shows the XRD patterns of the magnetron-deposited and electroplated Cr coatings with different thickness. The peaks of the substrate were not observed due to the limited penetration depth of X-rays. All coatings have body centered cubic (bcc) structure (α-Cr) and the XRD spectra show the (110), (200) and (211) reflections. The calculations of texture coefficients (Table 3) show that the magnetron-deposited Cr coatings have preferred (110) and (200) orientations.

Table 3
– The texture coefficients of the Cr coatings.

	M4.5	M6	M8.2	E5	E11	E15
T_c(110)	0.5	1.1	1.1	1.0	1.2	1.1
T_c(200)	2.0	1.3	1.4	0.5	0.4	0.4
T_c(211)	0.5	0.6	0.5	1.6	1.4	1.5

These samples had T_c(110) and T_c(200) coefficients as 0.5–1.1 and 1.3–2.0, while T_c(211) was only 0.5–0.6. In addition, the electroplated coatings have grown along (110) and (211) directions. For these samples, the values of T_c(110) and T_c(211) were 1.0–1.1 and 1.4–1.6, while T_c(200) had the lowest values (0.4–0.5).

It should be noted that the diffraction peaks of the electroplated Cr coatings are significantly broader than those of the magnetron coatings indicating smaller crystallites and higher microstrains.

Fig. 3,c shows the diffraction pattern of the E110 alloy after the surface activation during the electroplating process. The treatment of Zr alloy in fluoride salts and sulfuric acid solution etches the surface dissolving the native oxides and it leads to the formation of zirconium hydride γ-ZrH (PDF 00–034-0690), sodium zirconium fluorides $Na_5Zr_2F_{13}$ (PDF 04–013-9713) and Na_3ZrF_7 (PDF 04–011-2543) which prevent a further surface oxidation [38,45,46].

Based on the XRD tests, the residual stress in the M4.5 coating was compressive. It was equal to −4.4 and − 2.9 GPa for Cr(110) and Cr (200). While the E5 coating had −0.6 and 0.3 GPa for Cr(110) and Cr (211). The tensile stresses are usually observed for the electroplated chromium coatings [47].

Fig. 4 displays hardness (H) and elastic modulus (E) of the Cr coatings deposited by magnetron sputtering and electroplating. Both types of coatings have significant higher hardness and elastic modulus compared

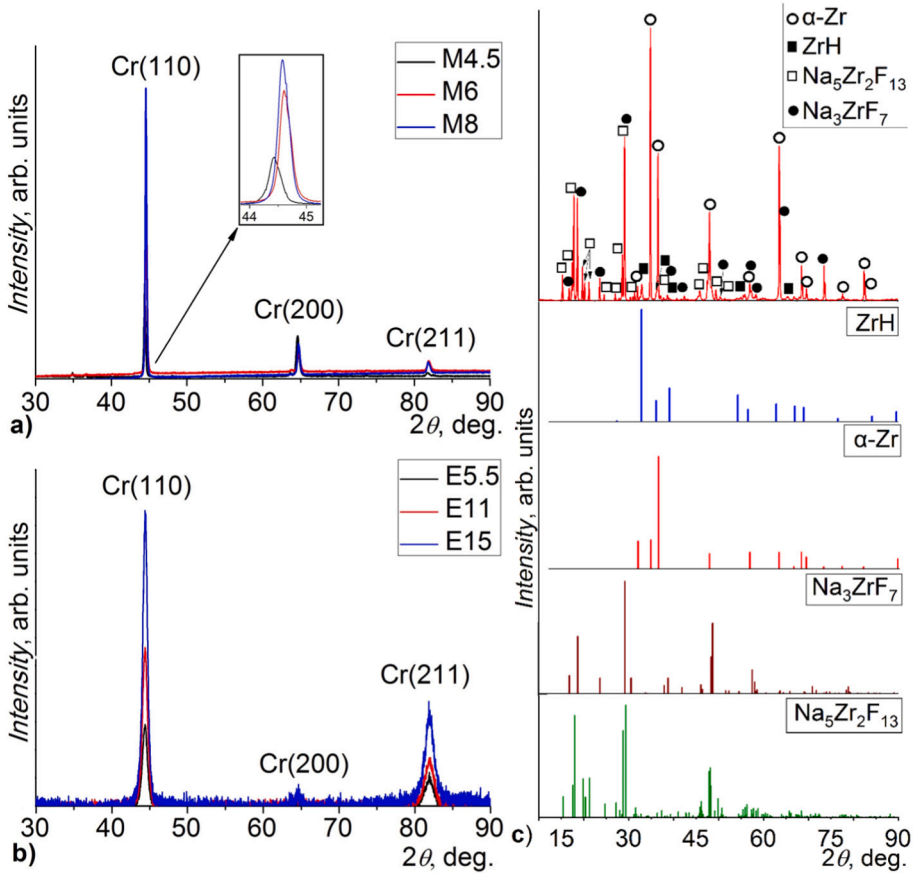

Fig. 3. XRD patterns of the as-deposited Cr coatings obtained by (a) magnetron sputtering and (b) electroplating with different thickness. (c) XRD pattern of the E110 alloy after surface activation during the electroplating process.

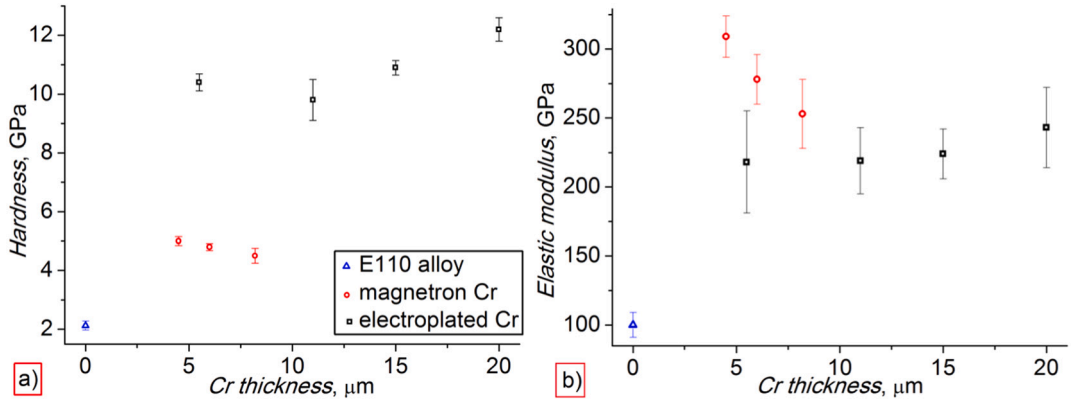

Fig. 4. Hardness (a) and elastic modulus (b) of the E110 alloy and Cr coatings deposited by magnetron sputtering and electroplating.

to E110 alloy which values of *H* and *E* are 2 and 100 GPa, respectively. The magnetron-deposited Cr coatings have a hardness of 4.5–5.1 GPa and elastic modulus of 253–309 GPa and both parameters decrease with the coating thickness. The electroplated Cr coatings show higher hardness and lower *E* modulus, increasing from 9.8 to 12.2 GPa by increasing the thickness, and from 218 to 243 GPa, respectively.

Fig. 5 shows the results of adhesion tests of the electroplated and magnetron-deposited Cr coatings (#E5, #M4.5). Similar data are obtained for the other samples with higher coating thickness. The magnetron-deposited coating is adherent to the substrate up to 30 N load. The signal of acoustic emission is lower and smoother in comparison with the electroplated Cr coatings. The optical images of the scratch track of the magnetron-deposited coating do not present any coating spallation or delamination, and the samples with higher coating thickness (6.0 and 8.2 μm) show a similar behavior.

The electroplated Cr coatings have a poor adhesion to the E110 alloy. The optical microphotographs showed that coating spallation began at *Fn* of 7.5 N and it is visible until the end of the scratch track. The electroplated coatings with higher thickness (#E11 and #E15) have also lower adhesion compared to magnetron-deposited ones since the spallation was observed at 8.2–11.8 N.

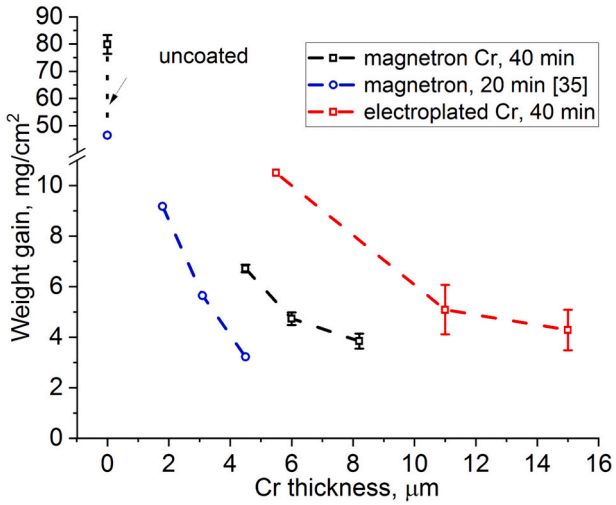

Fig. 6. The weight gains of the uncoated and Cr-coated E110 alloy after oxidation in air at 1100 °C for 40 min.

3.2. Weight gain measurements

The weight of the Cr-coated samples was measured before and after the oxidation test considering the geometry of the samples (coated and uncoated area). The samples had an uncoated area (~5–10 mm^2) due to its fixation to the substrate holder during the deposition. The weight gain is calculated according to the procedure described in the previous study (eq. (1) in ref. [35]).

Fig. 6 shows the weight gains of the uncoated and Cr-coated E110 alloy after oxidation in air at 1100 °C for 40 min. Additional data from [35] on the oxidation for 20 min are showed in Fig. 6. Similar to the previous study, the Cr-coated E110 alloy has lower weight gains in comparison with the uncoated sample (~79.9 mg/cm^2). Nevertheless, the weight gain of the Cr-coated E110 alloy has different behavior depending on the coating thickness and deposition technology. The weight gain decreases monotonically from 6.7 (4.5 μm) to 3.9 mg/cm^2 (8.2 μm) by increasing the thickness of magnetron-deposited coatings. For Cr electroplating, the weight gain has the same behavior (10.5 →

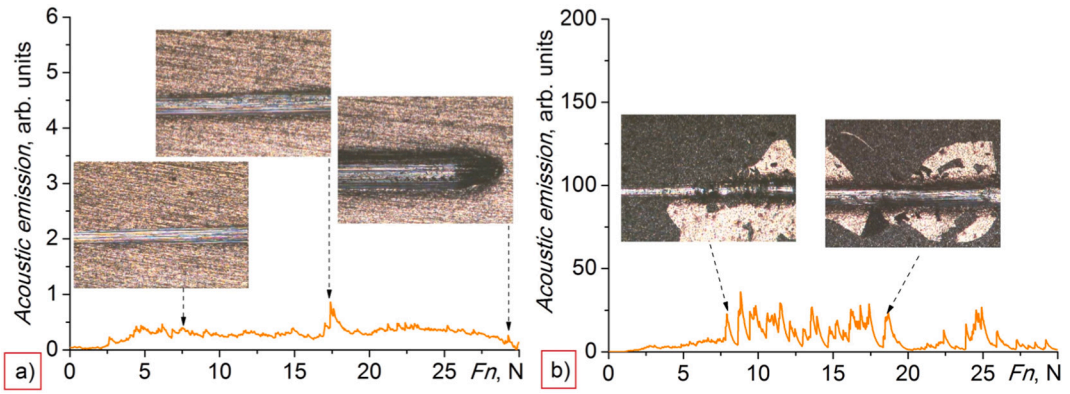

Fig. 5. Scratch tracks after adhesion tests of the as-deposited Cr coatings obtained by (a) magnetron sputtering and (b) electroplating (*Fn* – a normal force).

4.3 mg/cm^2), when the thickness of electroplated Cr coatings is increased (5.5 → 15.0 μm). However, the weight gain and its scatter are higher for the samples with electroplated Cr coatings than that of magnetron-deposited coatings.

3.3. The structure and phase composition of the oxidized samples

The outer views of the uncoated and Cr-coated E110 alloy after oxidation are shown in Fig. 7. The uncoated alloy has a white color on the whole surface due to oxidation of zirconium to ZrO_2. This sample is strongly cracked and a lot of pieces are spalled during the test. Oppositely, the Cr-coated E110 alloy preserves its integrity. All Cr-coated samples have dark-green/blue-grey color indicating the formation of chromia on the surface (Fig. 7,b and 7,c).

Fig. 8 shows the XRD patterns of the E110 alloy with the magnetron-deposited and electroplated Cr coatings after the oxidation test. All Cr coatings are partly oxidized to Cr_2O_3 since both reflections of residual bcc Cr and Cr_2O_3 phases are clearly visible. Moreover, α-Zr and ZrO_2 phases are observed in the #M4.5 sample indicating oxidation of E110 alloy, while the Cr_2Zr phase was formed due to Cr—Zr interdiffusion (Fig. 8,a). Only bcc Cr and Cr_2O_3 phases are observed with the thickest magnetron coating due to the limited X-ray penetration depth (Fig. 8,b). Similar to the magnetron-deposited coatings, Cr—Zr interdiffusion occurs in the electroplated samples since the Cr_2Zr phase is observed also for thicker coatings (Fig. 8,c and 8,d). Zirconium oxide/nitride phases are observed in all the electroplated coatings indicating that they are not fully protective. According to the XRD patterns, ZrO_2 and ZrN intensities are strongly decreased with the coating thickness and this is associated to higher absorption of X-rays.

An additional experiment was performed to understand the behavior of zirconium hydride and fluoride phases under high-temperature oxidation. For this, the #E15 sample was mechanically polished to delete Cr_2O_3 and Cr layers, then the sample was analyzed by XRD (Fig. 9) using the same conditions as above. According to the XRD pattern, the #E15 sample with electroplated Cr coating did not show any presence of γ-ZrH or sodium zirconium fluorides ($Na_5Zr_2F_{13}$ and Na_3ZrF_7) phases as before the oxidation test. The sample was only composed of ZrN, ZrO_2, Cr_2Zr and α-Zr(O)/α-Zr(N) phases.

The optical images of cross-sections of the uncoated and Cr-coated E110 alloy after the oxidation test are shown in Fig. 10. Several optical resolutions are used to display the general view of the samples and their microstructure at the surface. The uncoated E110 alloy is strongly oxidized at both sides (Fig. 10,a and 10,b). Its microstructure consists of (1) outer uneven ZrO_2/ZrN layer with a thickness up to 850 μm, (2) 40 μm-thick α–Zr(O)/α–Zr(N) layer and (3) internal prior β–Zr phase with α–Zr(O)/α–Zr(N) grains. Moreover, gold-colored ZrN phase is represented at the interface between the ZrO_2 and the α–Zr layers, as it is shown in Fig. 10,b.

The #M8.2 sample is fully protective at 1100 °C for 40 min since any presence of oxides or nitrides zirconium phases were found in the E110 alloy. The alloy remains in a prior β–Zr state, while the outer Cr coating is oxidized to Cr_2O_3. Underneath, the same sample has shown the presence of uniform residual Cr and Cr—Zr interlayers at the "coating-alloy" interface indicating the uncomplete oxidation of the Cr coating. The samples with lower Cr thickness are not fully protective against oxidation at 1100 °C for 40 min, this is also confirmed by the XRD studies. The #M6 sample has a α–Zr(O)/α–Zr(N) layer (5–20 μm), whereas the #M4.5 sample has ZrO_2 (5–10 μm) and thin α–Zr(O)/α–Zr(N) layers. The mentioned results show better protection properties of thicker magnetron-deposited coatings, in agreement with the result found in 20 min oxidation test [35].

The optical images of the #E15 sample present the typical microstructure of all electroplated E110 samples. This analysis revealed an inhomogeneous oxidized layer with local areas of zirconium oxides and nitrides (Fig. 10,e-10,g). Therefore, two types of microstructures are observed. The first type is consisted of ZrO_2 + ZrN/α-Zr(O) + α-Zr(N) layers. It is most likely that spallation of Cr_2O_3 and residual Cr layers occurred during preparation (grinding and polishing) procedure of cross-section of the oxidized samples. For the second type, the Cr coating is still adherent and protective, so microstructure in this region is similar to the magnetron-deposited ones. Moreover, it is important to note that accelerated oxidation in local regions can be caused by poor coating adhesion of the electroplated coatings.

Fig. 11 shows the cross-section microstructure and depth distributions of Zr, O and N in the uncoated E110 alloy after the oxidation in air.

The concentration of O had a near-constant behavior in the ranges of 0–700 and 1600–2000 μm in the cross-section of the uncoated alloy. In these regions, the oxygen concentration was higher60 at.%. This confirms the growth of thick ZrO_2 layers at both sides of the sample. At higher depths, between 850 and 1400 μm, the oxygen concentration decreased to ~2–5 at.%. The presence of O concentration of ~20 at.% (750–800 and 1450–1500 μm) indicates the stabilization of α–Zr(O) phase underneath the ZrO_2 layers. The N concentration was lower than that of O in the uncoated alloy after the oxidation. The N concentration was ~2–4 at.% along the depth profile of the cross-section. However, several maxima of the N concentration (6–8 at.%) were found in the ZrO_2 layers (at ~200, 380 and 1800 μm). Moreover, the significant increase of the N concentration to 11–16 at.% was observed in the ranges of 550–650 and 1550–1600 μm. It points at that the ZrN phase is predominantly disposed at the interface of ZrO_2 layer and Zr alloy.

The cross-section microstructure and EDS maps of the magnetron-deposited samples demonstrate that the #M8.2 sample was protective even after high-temperature oxidation for 40 min (Fig. 12). A Cr_2O_3 layer with a thickness of ~5 μm was observed at the surface region of the sample. Below this chromia layer, the residual Cr with a thickness of 2.5–3.2 μm was still present. Underneath the Cr layer, weak signals of Cr and Zr indicated the formation of intermetallic compounds layer with a thickness of 1.5–2.5 μm due to Cr—Zr interdiffusion.

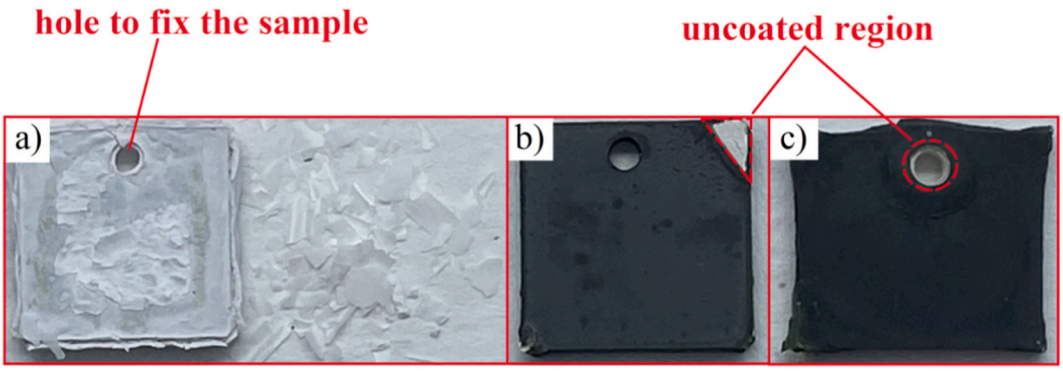

Fig. 7. The outer view of the E110 alloy after the oxidation test: a – uncoated; b – with magnetron-deposited Cr coating; c – with electroplated Cr coating.

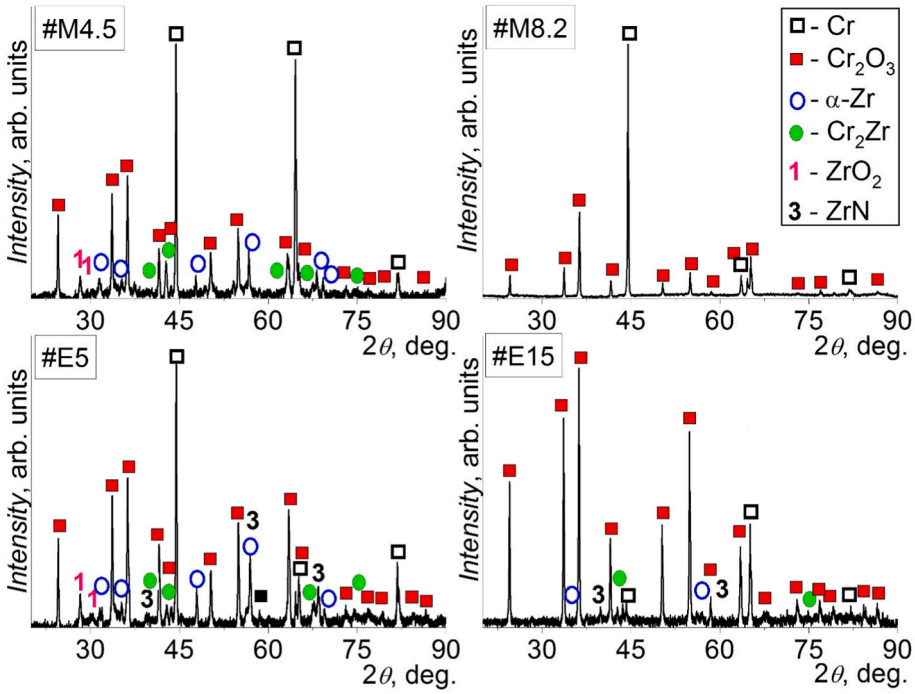

Fig. 8. The XRD patterns of the Cr-coated E110 alloy after the oxidation test: #M4.5, #M8.2 – with the magnetron Cr coatings; #E5, #E15 – with the electroplated Cr coatings.

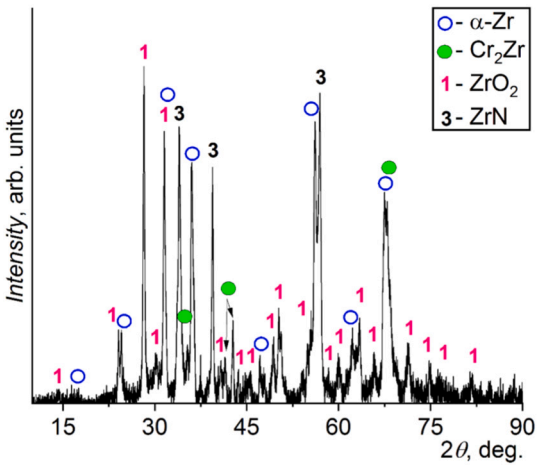

Fig. 9. The XRD pattern of the #E15 sample after the oxidation test.

The cross-section microstructure of the #E15 sample is shown in Fig. 13,a. As it was discussed above, the electroplated Cr coatings had poor adhesion to the E110 alloy, so they were partially spalled and cracked during polishing procedure. The multilayered structure formed at the surface is similar to that of the magnetron-deposited coatings. It indicates that the electroplated Cr coatings can have be protective under the high-temperature oxidation at 1100 °C in air, when their adhesion behavior will be significant enhanced. For further analysis of sodium zirconium fluorides and zirconium hydride behavior after high-temperature oxidation, EDS line-scanning in two zones of the #E15 sample (the protective zone in Fig. 13,b and oxidized zone in 13,c) and GDOES measurements of the #E15 sample (Fig. 14) were performed.

In the first case (Fig. 13,b), the formation of the outer Cr_2O_3, residual Cr and interdiffusion Cr_2Zr layers was observed, which is similar to the samples with the protective magnetron-deposited coatings. However, the Cr—Zr interlayer had more porous and cracked microstructure compared with the magnetron-deposited coatings. In the oxidized zone, the signals of O, N and Zr indicated the growth of ZrO_2 and ZrN layers at surface of the samples and α-Zr(O)/α-Zr(N) layer at higher depths.

According to the EDS line-scans in both protective and oxidized zones, the signals of Cr are found at depths higher than the coating thickness. Such signals are clearly pronounced at ~20 and 60 μm. In these areas, the content of Cr does not exceed 4–8 at.%. The content of Na and F is not more than ~2.5 and 1.5 at.% in the E110 alloy up to 100 μm in depth. Their concentration became lower than in the as-received samples (Fig. 2,d). Moreover, both Na and F signals have a low values up to a depth of ~8 μm in the protective zone of the #E15 sample (Fig. 13, b). This well correlates to the thickness of Cr_2O_3 and Cr layers.

Fig. 14 presents the GDOES-depth distributions of elements in the #E15 sample before and after the oxidation test.

As the content of Na and F was low, these elements were not detected in the #E15 sample by GDOES technique. However, the change of H depth distribution in the Zr alloy before and after the oxidation is found. Initially hydrogen was underneath the electroplated Cr coating in a thin layer (~5–7 μm) of the Zr alloy, while the penetration depth of H was up to ~120 μm after the oxidation test. Moreover, the slow increase of the Zr signal was detected up to the same depth and then the signal had a plateau. The depth distributions of O and N indicate their diffusion into the Zr alloy that can also influence the shape of the Zr signal. The maximums of O and N signals points to the forming the outer Cr_2O_3 layer and ZrO_2/ZrN layer at the "coating-alloy" interface, while the falling parts of the curves indicate the O- and N-stabilized α-Zr layer from 30 to 70 μm. The observed depth distributions of elements are well correlated with the previous data of the analysis of cross-section microstructure and crystal structure.

4. Discussion

Magnetron sputtering and electroplating were used to deposit Cr coatings on the E110 alloy. Both types of as-deposited coatings have a dense microstructure, but different mechanical properties and adhesion behavior.

The Ar^+ etching, substrate heating and biasing resulted in high-quality pretreatment procedure for a subsequent magnetron

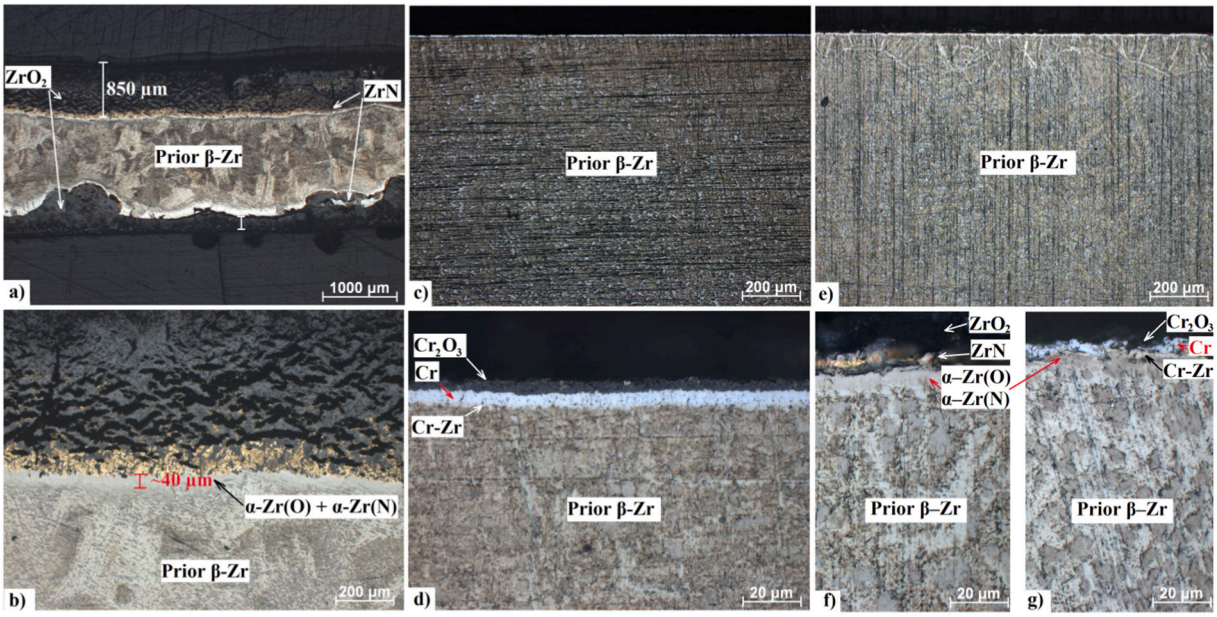

Fig. 10. Optical images of the cross-section of the oxidized samples: uncoated (a, b) and Cr-coated E110 alloy by magnetron sputtering (#M8.2 sample - c, d) and electroplating (#E15 sample - e, f and g).

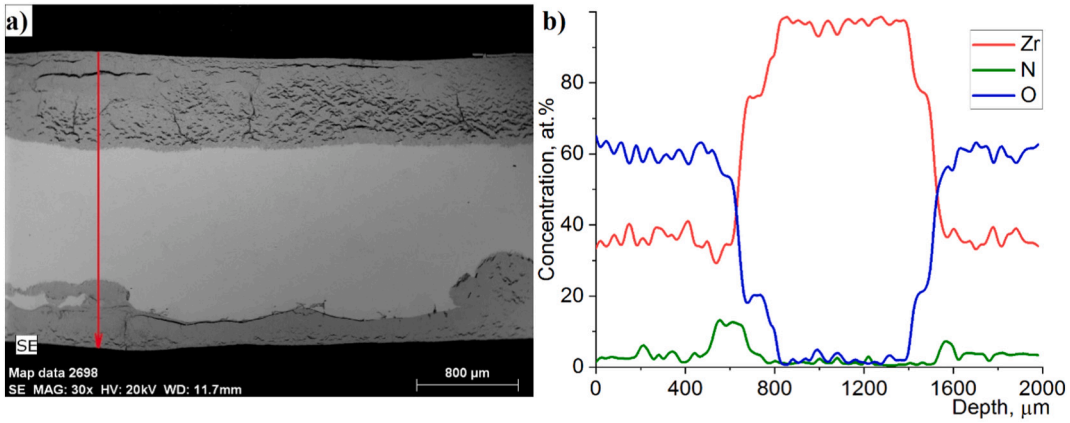

Fig. 11. (a) Cross-section microstructure and (b) depth distributions of Zr, O and N in the uncoated E110 alloy after the oxidation test.

deposition of Cr coatings on zirconium alloy. The magnetron-deposited coatings are fully adherent in the considered range of the applied load (up to 30 N), no any spallation and delamination were observed. By taking into account the mechanical properties (*H* and *E*), these coatings deposited on the E110 alloy have a typical adhesion behavior of "soft coating - soft substrate" system [48]. Oppositely, the electroplated Cr coatings have low adhesion even at the initial range of applied loads. Coating spallation began at 7.5–11.8 N and continued during the adhesion test that can be caused by several aspects. The first is the use of surface activation procedure that aims to avoid the formation of surface tenacious oxides on the E110 alloy prior to Cr electroplating process. In this case, a non-uniform (7–12 μm) interlayer containing hydride and fluoride phases with cracks and defects is formed between the Cr coating and E110 alloy. The second aspect is associated with the high hardness (9.8–12.2 GPa) and low elastic modulus (218–248 GPa) of the Cr coatings. Thus, the electroplated Cr coatings on the E110 alloy have a typical behavior of "hard coating – soft substrate" [48]. It results in low adhesion and spallation of the electroplated Cr coatings due to their lower plastic deformation in comparison to that of soft Zr alloy.

The uncoated E110 alloy was crucial oxidized in air at 1100 °C. The analysis of cross-section microstructure showed the growth of thick ZrO_2 layers at both sides of the alloy with embedded ZrN grains. The non-uniformity of the alloy oxidation was caused by "nitrogen effect" described in detail in [49,50]. The distributions of ZrO_2, ZrN and α-Zr over the cross-section confirmed the oxidation mechanism of Zr alloys in a nitrogen-containing atmosphere [51]. Since oxygen has high diffusion coefficient in zirconium, α-Zr(O) solid solution is initial formed under high-temperature oxidation. According to $P(O_2)/P(N_2)$ stability diagram for Zr, ZrN and ZrO_2 [52], zirconium nitride phase can be stable at very low oxygen partial pressures. Thus, ZrN can grow only in α-Zr(O) layer after full consumption of O by alloy. Moreover, α-Zr(O) has high nitriding kinetics [53]. The conditions for ZrN growth are fulfilled at the "oxide-alloy" interface. As oxygen continues to penetrate in the alloy, ZrN phase re-oxidized to ZrO_2 resulting in significant increase of molar volume (~48%) causing the cracking of oxide layer. The "nitrogen effect" causes both highly inhomogeneous oxidation of Zr alloys and the change from sub-parabolic to near-linear oxidation kinetics [54].

The Cr coating deposition can significantly improve oxidation resistance of zirconium alloys. However, the microstructure and adhesion of the Cr-coatings strongly influence its oxidation behavior in relation to the deposition technology. The thick magnetron-deposited Cr coatings were able to protect the E110 alloy from oxidation at 1100 °C

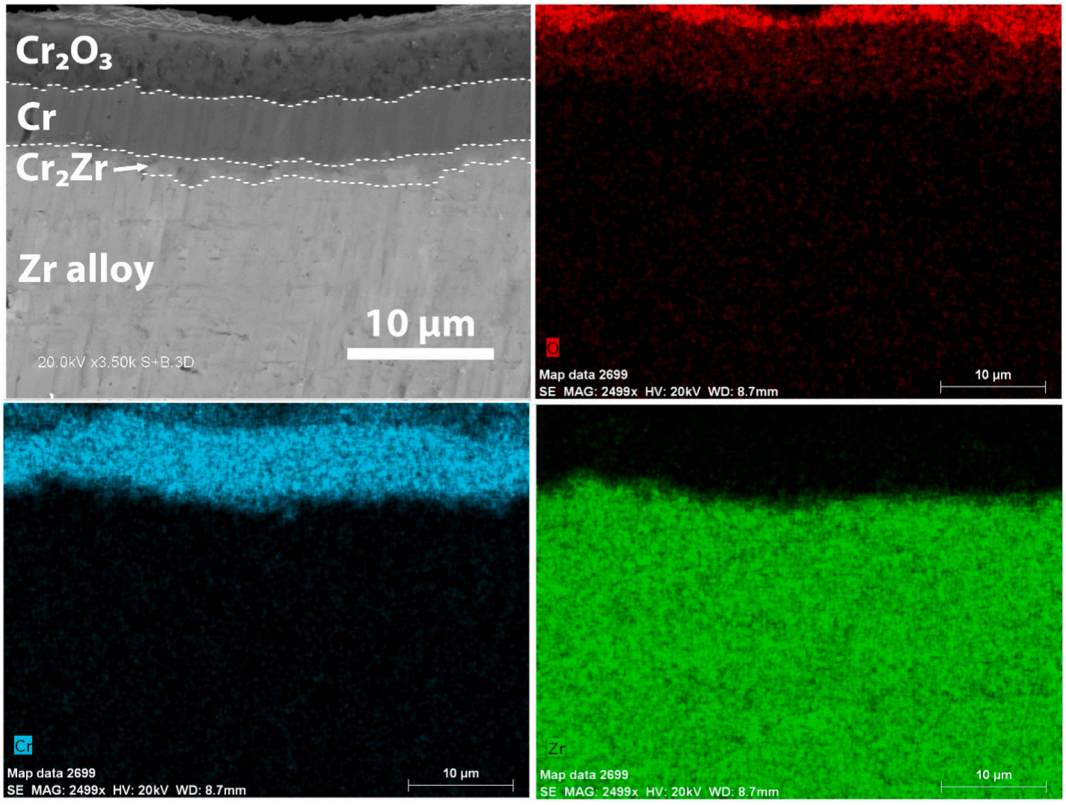

Fig. 12. Cross-section microstructure and EDS maps of the #M8.2 sample after the oxidation.

for 40 min, whereas the electroplated coatings resulted in less protective properties. Moreover, the resistance to oxidation of the magnetron-deposited Cr films was improved as their thickness increased from 4.5 to 8.2 μm, which is clearly visible from Fig. 6 and previous studies [3,4,24,35]. Both good adhesion and dense coating microstructure provides a stable and predictable behavior of the Cr coatings during oxidation that is well confirmed by cross-section microstructure (Fig. 10, c and 10,d). According to Fig. 12, the formation of Cr_2O_3 layer at the outer surface of the samples and interdiffusion of Cr—Zr at the "coating-alloy" interface leaded to the growth of Cr_2Zr phase. Cr coatings are protective until oxygen does not reach the Zr alloy. The consumption of Cr coating by Cr—Zr interdiffusion leads to decrease of the diffusion path of O toward the alloy, so thicker coatings should be used to increase the duration of protective period. The obtained conclusions are correlated with the oxidation mechanism of PVD Cr-coated zirconium alloys in air and steam that have been discussed in detail in recent studies [4,24,35,48].

The electroplated Cr samples showed less uniform and stable oxidation behavior under high-temperature oxidation in air (Fig. 10,e-10,g) that also confirms by the weight gain of the samples after the oxidation tests (Fig. 6). The local oxidation of the electroplated Cr samples and the presence of defects at the "coating-alloy" interface in the as-deposited samples indicated the critical role of the interlayer during the oxidation (Fig. 13,b). In the regions where the coating was still adherent to the alloy, the samples had the protective scale similar to the magnetron-deposited ones. The electroplated Cr coatings had low compressive (−0.6 GPa) and tensile (0.3 GPa) stresses for Cr(110) and Cr (221) peaks, respectively. It results in low adhesion of the electroplated Cr coatings (Fig. 5,b). The low adhesion of electroplated Cr coatings caused a local oxidation of the zirconium alloy that is clearly observed in Fig. 13,c. Thus, PVD Cr coatings exhibit better oxidation resistance than the electroplated ones. The development of new methods of surface pretreatment of Zr alloys prior to Cr electroplating or improvements of the electrolyte composition are necessary to improve the adhesion and to reduce defects at the "coating-alloy" interface.

According to XRD analysis of the electroplated samples after oxidation (Fig. 9), SEM observations (Fig. 13) and GDOES-depth distributions (Fig. 14), it is speculated that decomposition of zirconium hydride and fluoride phases followed by dissolution of H, Na and F in the Zr alloy. The additional attention should be devoted to zirconium hydride behavior during the oxidation test. As the temperature of the oxidation was higher than that of ZrH decomposition (at ~825 °C [55]), zirconium hydride can decompose during the heating and isothermal stages of the oxidation test and then H dissolves in the Zr alloy. As the Cr coatings have low hydrogen permeability and can work as the barrier layer for H [20], hydrogen penetrates at higher depth than that of before the oxidation. Then, zirconium hydrides can be formed in the α-Zr alloy matrix [56] at the cooling stage of the oxidation test. However, the hydrides are non-uniform distributed over a depth that is well seen from the H and Zr depth distributions in the #E15 sample after the oxidation (Fig. 14).

In summary, deposition technologies of Cr coating on Zr alloys have been compared and discussed. Both technologies have been used for a long time, technical solutions are already been existing for coating deposition on components such as tubes and pipes. However, sputtering and electroplating are significantly different by technical requirements, productivity and cost. Magnetron sputtering requires vacuum system, periodic cleaning of vacuum chamber and technological devices as well as 3D scanning for uniform deposition of coatings on tube-shape components. Considering the above requirements, the cost of magnetron-deposited coatings is rather higher than electroplated ones. On the other hand, the obtained results as well as the data of other authors [3–8,20,21] show that magnetron deposition technology is very promising for production of Cr-coated Zr claddings. At the same time, electroplating has high productivity since no vacuum system is needed that also provides a low deposition cost. Among the disadvantages of Cr electroplating, several factors should be mentioned. Firstly, it is the use of chemical reagents, which application and disposal is not

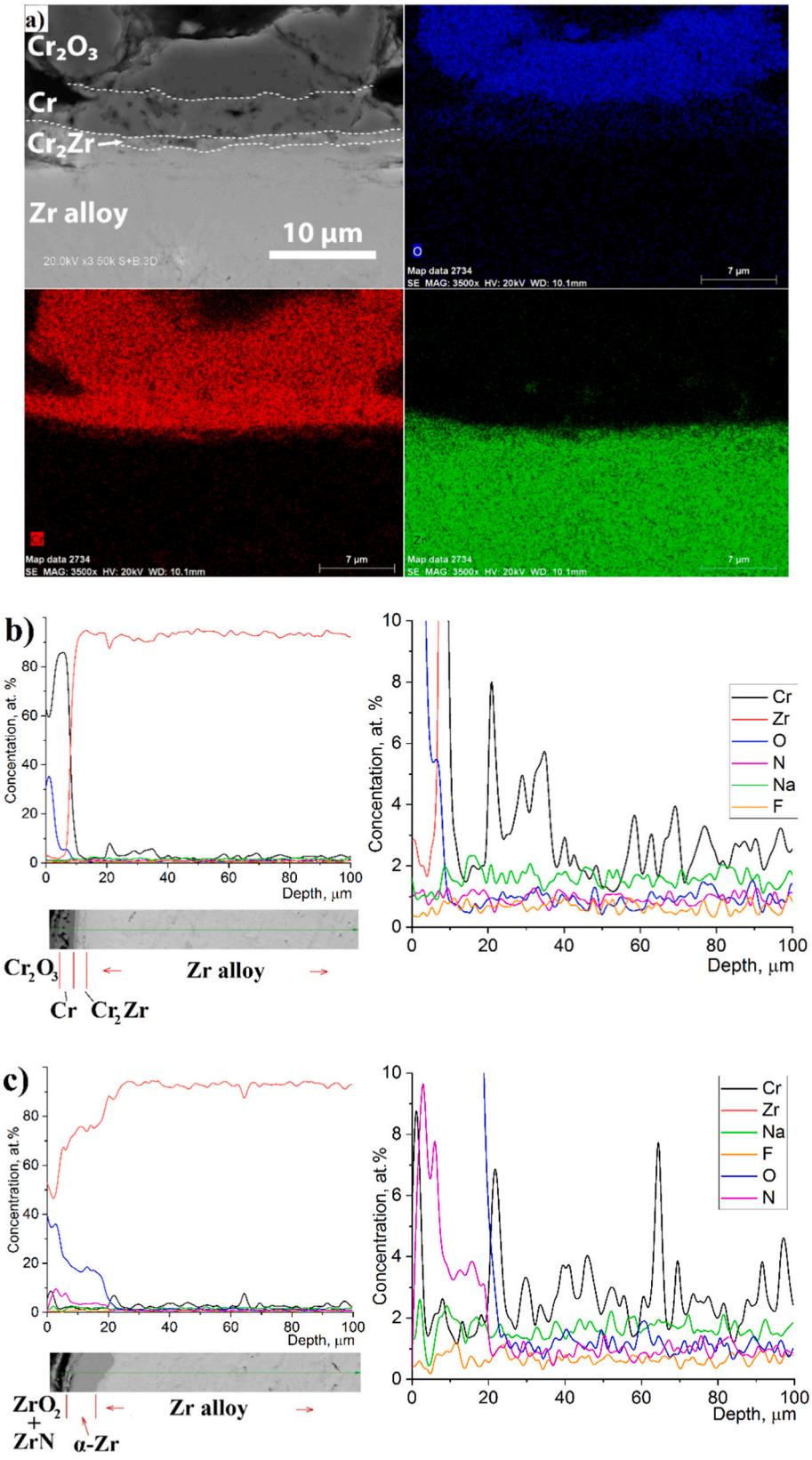

Fig. 13. (a) Cross-section microstructure and EDS maps of the #E15 sample after the oxidation test. EDS line-scans in (b) protective and (c) oxidized zones of the #E15 sample.

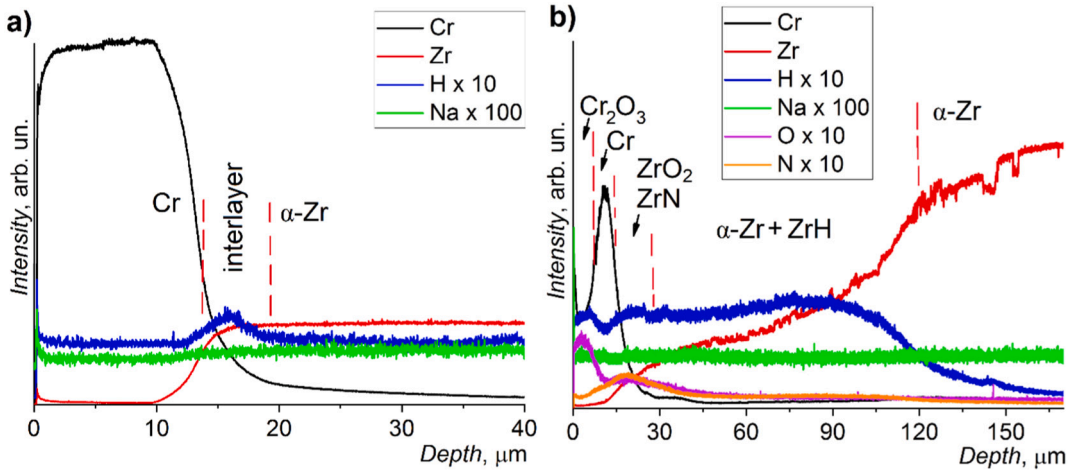

Fig. 14. Depth distributions of elements in the #E15 sample (a) before and (b) after the oxidation.

environmentally friendly. Secondly, the activation procedure to remove of tenacious surface oxides on Zr alloys should be improved. The Cr—Zr interdiffusion phenomena is crucial for the selection of coating deposition technology. Nowadays, different barrier layers are studied to prevent the formation of eutectic phase [57–59]. It is most likely that bilayer or multilayer coatings mitigating interdiffusion can be beneficial under beyond-design basis accident conditions. For their deposition, magnetron sputtering is more appropriate.

Despite the above advantages and disadvantages, the authors assume that both deposition technologies can be applied for production of ATF fuel claddings. Magnetron sputtering seems to be better for deposition of Cr-based coatings on Zr claddings. In turn, Cr electroplating can be effective for deposition of Cr coatings on spacer grits, which are used as a construction element of fuel assembly and have a complex geometry.

5. Conclusions

Magnetron sputtering and electroplating were used to deposit the Cr coatings on E110 alloy. The properties of the as-deposited coatings and resistance of the Cr-coated alloy to high-temperature oxidation (1100 °C) in air were studied.

1. Magnetron-deposited Cr coatings have uniform and dense microstructure as well as good adhesion to E110 alloy. The oxidation resistance of the alloy with magnetron-deposited coating increased with their thickness.
2. The magnetron Cr coatings have stable and predictable oxidation behavior. Despite lower thickness, this coating type has better oxidation resistance in comparison with the electroplated coatings.
3. The electroplating of Cr on E110 zirconium alloy requires the use of special activation procedure to avoid the formation of surface oxide. This results in formation of the non-uniform interlayer (~7–12 μm) containing hydride and fluoride phases at the coating/alloy interface. The presence of cracks and non-regularities in the interlayer and the brittleness of the electroplated chromium cause a lower adhesion and oxidation resistance regardless the dense microstructure of the coating.
4. New pretreatment procedures of Zr alloys before Cr electroplating or changes in the bath composition or post-treatment procedures of Cr-coated Zr alloys could be considered to improve the coating adhesion and its oxidation behavior.

Funding

The work was supported by the Russian Science Foundation [grant no. 19-79-10116].

CRediT authorship contribution statement

Dmitrii V. Sidelev: Conceptualization, Investigation, Methodology, Formal analysis, Writing - Original draft preparation, Funding acquisition.

Cristiano Poltronieri: Investigation, Formal analysis, Writing - Reviewing and Editing.

Massimiliano Bestetti: Conceptualization, Formal analysis, Writing - Original draft preparation.

Maxim G. Krinitcyn: Investigation.

Vladislav A. Grudinin: Visualization, Investigation.

Egor B. Kashkarov: Investigation, Writing - Reviewing and Editing.

Declaration of competing interest

The authors declare that they have no known competing financial interests or personal relationships that could have appeared to influence the work reported in this paper.

Acknowledgements

The authors acknowledge the TPU Enhancement Program.

References

[1] N. Minin, T. Vlček, Post-Fukushima performance of the major global nuclear technology providers, Energ. Strat. Rev. 21 (2018) 98–110, https://doi.org/10.1016/j.esr.2018.05.006.
[2] M. Steinbrück, Hydrogen absorption by zirconium alloys at high temperatures, J. Nucl. Mater. 334 (2004) 58–64, https://doi.org/10.1016/j.jnucmat.2004.05.007.
[3] J.C. Brachet, I. Idarraga-Trujillo, M. Le Flem, M. Le Saux, V. Vandenberghe, et al., Early studies on Cr-coated Zircaloy-4 as enhanced accident tolerant nuclear fuel claddings for light water reactors, J. Nucl. Mater. 517 (2019) 268–285, https://doi.org/10.1016/j.jnucmat.2019.02.018.
[4] J.C. Brachet, E. Rouesne, J. Ribis, T. Guilbert, S. Urvoy, G. Nony, et al., High temperature steam oxidation of chromium-coated zirconium-based alloys: kinetics and process, Corros. Sci. 167 (2020), 108537, https://doi.org/10.1016/j.corsci.2020.108537.
[5] J. Krejcí, J. Kabátová, F. Manoch, J. Kočí, L. Cvrček, J. Málek, et al., Development and testing of multicomponent fuel cladding with enhanced accidental performance, Nucl. Eng. Technol. 52 (2020) 597–609, https://doi.org/10.1016/j.net.2019.08.015.
[6] J. Bischoff, et al., AREVA NP's enhanced accident-tolerant fuel developments: focus on Cr-coated M5 cladding, Nucl. Eng. Technol. 50 (2018) 223–228, https://doi.org/10.1016/j.net.2017.12.004.
[7] C. Tang, M. Stueber, H.J. Seifert, M. Steinbrueck, Protective coatings on zirconium-based alloys as accident-tolerant fuel (ATF) claddings, Corros. Rev. 35 (2017) 141–165, https://doi.org/10.1515/corrrev-2017-0010.
[8] H. Kim, J. Yang, W. Kim, Y. Koo, Development status of accident-tolerant fuel for light water reactors in Korea, Nucl. Eng. Technol. 48 (2016) 1–15, https://doi.org/10.1016/j.net.2015.11.011.

[9] X. Wang, Y. Liao, C. Xu, H. Guan, M. Zhu, C. Gao, X. Jin, P. Pang, J. Du, B. Liao, E. Xue, Steam oxidation behavior of ZrO_2/Cr-coated pure zirconium prepared by plasma electrolytic oxidation followed by filtered cathodic vacuum arc deposition, J. Alloys Compd. 883 (2021), 160798, https://doi.org/10.1016/j.jallcom.2021.160798.

[10] D.V. Sidelev, M.S. Syrtanov, S.E. Ruchkin, A.V. Pirozhkov, E.B. Kashkarov, Protection of Zr alloy under high-temperature air oxidation: a multilayer coating approach, Coatings. 11 (2021) 227, https://doi.org/10.3390/coatings11020227.

[11] Q. Chen, H. Yang, L. Wu, X. Wu, C. Zhu, L. He, N. Liu, Y. Yang, J. Liao, J. Yang, Effect of the Ar/N2 flow ratio on the microstructure, mechanical properties, and high-temperature steam oxidation behavior of Cr/CrxN coatings for accident-tolerant fuel coatings, Corros. Sci. 192 (2021), 109833, https://doi.org/10.1016/j.corsci.2021.109833.

[12] W. Zhong, P.A. Mouche, X. Han, B.J. Heuser, K.K. Mandapaka, G.S. Was, Performance of iron–chromium–aluminum alloy surface coatings on zircaloy 2 under high-temperature steam and normal BWR operating conditions, J. Nucl. Mater. 470 (2016) 327–338, https://doi.org/10.1016/j.jnucmat.2015.11.037.

[13] K. Sridharan, S. Harrington, A. Johnson, J. Licht, M. Anderson, T. Allen, Oxidation of plasma surface modified zirconium alloy in pressurized high temperature water, Mater. Des. 28 (2007) 1177–1185, https://doi.org/10.1016/j.matdes.2006.01.019.

[14] W. Zhang, R. Tang, Z. Yang, C. Liu, H. Chang, J. Yang, J. Liao, Y. Yang, N. Liu, Preparation, structure, and properties of high-entropy alloy multilayer coatings for nuclear fuel cladding: a case study of AlCrMoNbZr/(AlCrMoNbZr)N, J. Nucl. Mater. 512 (2018) 15–24, https://doi.org/10.1016/j.jnucmat.2018.10.001.

[15] M.A. Tunes, F.C. Da Silva, O. Camara, C.G. Schön, J.C. Sagás, L.C. Fontana, S. E. Donnelly, G. Greaves, P.D. Edmondson, Energetic particle irradiation study of TiN coatings: are these films appropriate for accident tolerant fuels? J. Nucl. Mater. 512 (2018) 239–245, https://doi.org/10.1016/j.jnucmat.2018.10.013.

[16] E. Alat, A.T. Motta, R.J. Comstock, J.M. Partezana, D.E. Wolfe, Multilayer (TiN, TiAlN) ceramic coatings for nuclear fuel cladding, J. Nucl. Mater. 478 (2016) 236–244, https://doi.org/10.1016/j.jnucmat.2016.05.021.

[17] H. Yeom, B. Maier, R. Mariani, D. Bai, S. Fronek, P. Xu, K. Sridharan, Magnetron sputter deposition of zirconium-silicide coating for mitigating high temperature oxidation of zirconium-alloy, Surf. Coat. Technol. 316 (2017) 30–38, https://doi.org/10.1016/j.surfcoat.2017.03.018.

[18] K. Lee, D. Kim, Y.S. Yoon, SiC/Si thin film deposited on zircaloy to improved accident tolerant fuel cladding, Thin Solid Films 660 (2018) 221–230, https://doi.org/10.1016/j.tsf.2018.06.006.

[19] A. Michau, F. Maury, F. Schuster, F. Lomello, J.-C. Brachet, E. Rouesne, M. Le Saux, R. Boichot, M. Pons, High-temperature oxidation resistance of chromium-based coatings deposited by DLI-MOCVD for enhanced protection of the inner surface of long tubes, Surf. Coat. Technol. 349 (2018) 1048–1057, https://doi.org/10.1016/j.surfcoat.2018.05.088.

[20] D.V. Sidelev, E.B. Kashkarov, M.S. Syrtanov, V.P. Krivobokov, Nickel-chromium (Ni–Cr) coatings deposited by magnetron sputtering for accident tolerant nuclear fuel claddings, Surf. Coat. Technol. 369 (2019) 69–78, https://doi.org/10.1016/j.surfcoat.2019.04.057.

[21] K.A. Terrani, Accident tolerant fuel cladding development: promise, status, and challenges, J. Nucl. Mater. 501 (2018) 13–30, https://doi.org/10.1016/j.jnucmat.2017.12.043.

[22] X.G. Hu, C. Dong, Q. Wang, B.Q. Chen, H.Y. Yang, T.G. Wei, R.Q. Zhang, W. Gu, D. M. Chen, High-temperature oxidation of thick Cr coating prepared by arc deposition for accident tolerant fuel claddings, J. Nucl. Mater. 519 (2019) 145–156, https://doi.org/10.1016/j.jnucmat.2019.01.039.

[23] H.G. Kim, I.H. Kim, Y.I. Jung, D.J. Park, J.Y. Park, Y.H. Koo, Adhesion property and high-temperature oxidation behavior of cr-coated Zircaloy-4 cladding tube prepared by 3D laser coating, J. Nucl. Mater. 465 (2015) 531–539, https://doi.org/10.1016/j.jnucmat.2015.06.030.

[24] E.B. Kashkarov, D.V. Sidelev, M.S. Syrtanov, C. Tang, M. Steinbrück, Oxidation kinetics of Cr-coated zirconium alloy: effect of coating thickness and microstructure, Corros. Sci. 175 (2020), 108883, https://doi.org/10.1016/j.corsci.2020.108883.

[25] J.C. Brachet, A. Billard, F. Shuster, M. Le Flem, I. Idarraga-Trujillo, M. Le Saux, F. Lomello, Gaines de combustible nucleaire, procedes de fabrication et utilisation contre l'oxydation, brevet Français FR, 3025929B, 23/09/2014..

[26] X. Han, J. Xue, S. Peng, H. Zhang, An interesting oxidation phenomenon of Cr coatings on Zry-4 substrates in high temperature steam environment, Corros. Sci. 156 (2019) 117–124, https://doi.org/10.1016/j.corsci.2019.05.017.

[27] Q.S. Chen, C.H. Liu, R.Q. Zhang, H.Y. Yang, T.G. Wei, et al., Microstructure and high-temperature steam oxidation properties of thick cr coatings prepared by magnetron sputtering for accident tolerant fuel claddings: the role of bias in the deposition process, Corros. Sci. 162 (2020), 108378, https://doi.org/10.1016/j.corsci.2019.108378.

[28] J.-C. Brachet, I. Idarraga-Trujillo, M. Le Flem, M. Le Saux, V. Vandenberghe, S. Urvoy, E. Rouesne, T. Guilbert, C. Toffolon-Masclet, M. Tupin, Early studies on cr-coated Zircaloy-4 as enhanced accident tolerant nuclear fuel claddings for light water reactors, J. Nucl. Mater. 517 (2019) 268–285, https://doi.org/10.1016/j.jnucmat.2019.02.018.

[29] X. Wang, H. Guan, Y. Liao, M. Zhu, C. Xu, X. Jin, B. Liao, W. Xue, Y. Zhang, G. Bai, et al., Enhancement of high temperature steam oxidation resistance of Zr–1Nb alloy with ZrO2/Cr bilayer coating, Corros. Sci. 187 (2021), 109494, https://doi.org/10.1016/j.corsci.2021.109494.

[30] H. Yeom, K. Sridharan, Cold spray technology in nuclear energy applications: a review of recent advances, Ann. Nucl. Energy 150 (2021), 107835.

[31] H.-G. Kim, I.-H. Kim, Y.-I. Jung, D.-J. Park, J.-Y. Park, Y.-H. Koo, Adhesion property and high-temperature oxidation behavior of Cr-coated Zircaloy-4 cladding tube prepared by 3D laser coating, J. Nucl. Mater. 465 (2015) 531–539, https://doi.org/10.1016/j.anucene.2020.107835.

[32] M. Huang, Y. Li, G. Ran, Z. Yang, P. Wang, Cr-coated zr-4 alloy prepared by electroplating and its in situ He+ irradiation behavior, J. Nucl. Mater. 538 (2020), 152240, https://doi.org/10.1016/j.jnucmat.2020.152240.

[33] A.S. Kuprin, V.A. Belous, V.N. Voyevodin, V.V. Bryk, R.L. Vasilenko, V. D. Ovcharenko, E.N. Reshetnyak, G.N. Tolmachova, P.N. V'yugov, Vacuum-arc chromium-based coatings for protection of zirconium alloys from the high-temperature oxidation in air, J. Nucl. Mater. 465 (2015) 400–406, https://doi.org/10.1016/j.jnucmat.2015.06.016.

[34] G. Bräuer, B. Szyszka, M. Vergöhl, R. Bandorf, Magnetron sputtering – milestones of 30 years, Vacuum 84 (2010) 1354–1359, https://doi.org/10.1016/j.vacuum.2009.12.014.

[35] E.B. Kashkarov, D.V. Sidelev, M. Rombaeva, M.S. Syrtanov, G.A. Bleykher, Chromium coatings deposited by cooled and hot target magnetron sputtering for accident tolerant nuclear fuel claddings, Surf. Coat. Technol. 389 (2020), 125618, https://doi.org/10.1016/j.surfcoat.2020.125618.

[36] A.V. Kaziev, A.V. Tumarkin, K.A. Leonova, D.V. Kolodko, M.M. Kharkov, D. G. Ageychenkov, Discharge parameters and plasma characterization in a dc magnetron with liquid cu target, Vacuum 156 (2018) 48–54, https://doi.org/10.1016/j.vacuum.2018.07.001.

[37] A. Caillard, M. El'Mokh, T. Lecas, A.-L. Thomann, Effect of the target temperature during magnetron sputtering of Nickel, Vacuum 147 (2018) 82–91, https://doi.org/10.1016/j.vacuum.2017.10.016.

[38] J.W. Dini, H.A. Johnson, A. Jonas, Plating on Zircaloy-2, Sandia Laboratories, 1979.

[39] M. Huang, Y. Li, G. Ran, Z. Yang, P. Wang, Cr-coated zr-4 alloy prepared by electroplating and its in situ He+ irradiation behavior, J. Nucl. Mater. 538 (2020), 152240, https://doi.org/10.1016/j.jnucmat.2020.152240.

[40] M. Charveriat, U.S. Patent, 3,502,549, March 1970.

[41] J.W. Dini, H.R. Johnson, Plating on some difficult-to-plate metals and alloys, in: SAND79-8069, Sandia Laboratories, 1980.

[42] Z.B. Yang, J.J. Liao, S.Y. Qiu, Z.Q. Cheng, H. Liu, Z.P. Wu, J. Qiu, B. Gao, Effect of final annealing temperature on corrosion resistance of SZA-6 zirconium alloy cladding tubes, Mater. Sci. Forum 944 (2019) 488–498, https://doi.org/10.4028/www.scientific.net/MSF.944.488.

[43] Z. Duan, H. Yang, Y. Satoh, K. Murakami, S. Kano, Z. Zhao, J. Shen, H. Abe, Current status of materials development of nuclear fuel cladding tubes for light water reactors, Nucl. Eng. Des. 316 (2017) 131–150, https://doi.org/10.1016/j.nucengdes.2017.02.031.

[44] G.B. Harris, Quantitative measurement of preferred orientation in rolled uranium bars, Philos. Mag. A 43 (1952) 113–123, https://doi.org/10.1080/14786440108520972.

[45] K. Yokoyama, D. Yamada, J. Sakai, Corrosion and hydrogen absorption of commercially pure zirconium in acid fluoride solutions, Corros. Sci. 73 (2013) 375–381, https://doi.org/10.1016/j.corsci.2013.04.027.

[46] D. Hartshorn, US patent 3,725,217, 1970.

[47] J. Pina, A. Dias, M. Francois, J.L. Lebrun, Residual stresses and crystallographic in hard-chromium electroplated coatings, Surf. Coat. Technol. 96 (1997) 148–162, https://doi.org/10.1016/S0257-8972(97)00075-3.

[48] S.J. Bull, E.G. Berasetegui, An overview of the potential of quantitative coating adhesion measurement by scratch testing, Tribol. Internat. 39 (2006) 99–114, https://doi.org/10.1016/j.triboint.2005.04.013.

[49] M. Steinbrueck, F. Oliveira da Silva, M. Grosse, Oxidation of Zircaloy-4 in steam-nitrogen mixtures at 600–1200 °C, J. Nucl. Mater. 490 (2017) 226–237, https://doi.org/10.1016/j.jnucmat.2017.04.034.

[50] C. Duriez, D. Drouan, G. Pouzadoux, Reaction in air and in nitrogen of pre-oxidised Zircaloy-4 and M5™ claddings, J. Nucl. Mater. 441 (2013) 84–95, https://doi.org/10.1016/j.jnucmat.2013.04.095.

[51] M. Steinbrück, S. Schaffer, High-temperature oxidation of zircaloy-4 in oxygen-nitrogen mixtures, Oxid. Met. 85 (2016) 245–262, https://doi.org/10.1007/s11085-015-9572-1.

[52] I. Barin, Thermochemical Data of Pure substances, VCH Verlagsgesellschaft, Weinheim, 1995, https://doi.org/10.1002/9783527619825.

[53] M. Steinbrück, N. Ver, High-temperature oxidation of Zircaloy-4 in mixed steam-air and steam-nitrogen atmospheres, in: International Congress on Advances in Nuclear Power Plants 2010 2, ICAPP, 2010, pp. 1051–1061, 2010.

[54] M. Steinbrück, Prototypical experiments relating to air oxidation of Zircaloy-4 at high temperatures, J. Nucl. Mater. 392 (2009) 531–544, https://doi.org/10.1016/J.JNUCMAT.2009.04.018.

[55] E. Zuzek, J. Abriata, A. San-Martin, F. Manchester, The H-Zr (hydrogen-zirconium) system, Bull. Alloy Phase Diagr. 11 (1990) 385–395, https://doi.org/10.1007/BF02843318.

[56] T.B. Douglas, High-temperature thermodynamic functions for zirconium and unsaturated zirconium hydrides, J. Res. Natl. Bur. Stand. A Phys. Chem. 67A (1963) 403–426, https://doi.org/10.6028/jres.067A.043.

[57] E. Kashkarov, B. Afornu, D. Sidelev, M. Krinitcyn, V. Gouws, A. Lider, Recent advances in protective coatings for accident tolerant Zr-based fuel claddings, Coatings 11 (2021) 557, https://doi.org/10.3390/coatings11050557.
[58] J. Krejcí, J. Kabátová, F. Manoch, J. Kočí, L. Cvrček, J. Málek, S. Krum, P. Šutta, P. Bublíková, P. Halodová, Development and testing of multicomponent fuel cladding with enhanced accidental performance, Nucl. Eng. Technol. 52 (2020) 597–609, https://doi.org/10.1016/j.net.2019.08.015.
[59] X. Han, Y. Wang, S. Peng, H. Zhang, Oxidation behavior of FeCrAl coated Zry-4 under high temperature steam environment, Corros. Sci. 149 (2019) 45–53, https://doi.org/10.1016/j.corsci.2019.01.004.